Study of exciton-polariton modes in nanocrystalline thin films of CuCl using reflectance spectroscopy

Barry Foy,[1,a)] Enda McGlynn,[1,b)] Aidan Cowley,[2] Patrick J. McNally,[2] and Martin O. Henry[1]
[1]*School of Physical Sciences, National Centre for Plasma Science and Technology, Dublin City University, Glasnevin, Dublin 9, Ireland*
[2]*Nanomaterials Processing Laboratory, The Rince Institute, School of Electronic Engineering, Dublin City University, Dublin 9, Ireland*

(Received 2 May 2012; accepted 27 June 2012; published online 2 August 2012)

CuCl thin films grown on (100) Si by thermal evaporation are studied using reflectance spectroscopy. The reflectance spectra in the near UV spectral range close to the CuCl bandgap are modeled using a dielectric response function based on an exciton-polariton response with various models involving dead layers and reflected waves in the thin film. The exciton-polariton structure obtained is compared to other studies of bulk CuCl crystals. These different models are analyzed using a matrix-based approach and they yield theoretical spectra of reflected intensity. The fits provide parameter values which can be compared to bulk data known for CuCl and provide a non-destructive means of quantitative analysis of CuCl thin films. The best models are shown to match the experimental data quite well, with the closest fits produced when thin film front and rear interfaces are included. This model also accurately simulates the Fabry-Perot fringes present at energies lower than the Z_3 free exciton position in CuCl (at 3.272 eV). © *2012 American Institute of Physics*. [http://dx.doi.org/10.1063/1.4739726]

I. INTRODUCTION

Wide band gap materials have been studied extensively for a range of applications such as UV light emitting diodes, diode lasers, and detectors.[1] Most of these efforts have focused on II-VI and III-nitride material systems, with the latter being the most productive for applications to date. A fundamental problem with such systems however is the large lattice mismatch (~13%, Ref. 2) between the GaN epitaxial layers and common suitable substrates (e.g., SiC, α-Al_2O_3), which results in high densities of threading dislocations. With a band gap of 3.39 eV, a large exciton binding energy of 190 meV, and a lattice mismatch with Si of <0.4% at room temperature,[3] cubic CuCl shows great promise as a competitor material in this space. Furthermore, because CuCl is closely lattice-matched to both Si and GaAs, it is an ideal candidate for the development of hybrid electronic-optoelectronic platforms. The low lattice mismatch should allow for low defect density CuCl growth on such substrates. The optical properties of CuCl thin films and their detailed understanding and optimisation are key challenges to the development of potential uses of this material in optoelectronic devices.

Reflectance spectroscopy is a useful technique in the study of the optical properties of thin films as it allows one to deduce exciton energies, resonant damping/broadening coefficients, and to understand the effects of strain and other perturbations.[4–6] Previous studies of CuCl using reflectance have been performed either on bulk material[7] or CuCl microcavities.[8,9] The purpose of this paper is to report low temperature reflectance spectroscopic data from thin CuCl films on (100) Si substrates and to model the exciton-polariton structure underlying such phenomena.

The classical theory of exciton-polariton coupling given by Hopfield and Thomas[10] was used to model the reflectance data in the MATLAB programming environment.[11] Each of the experimental scans was performed at near normal incidence to minimize the influence of longitudinal exciton bands and allow our spectra to be modeled using a coupled two-exciton band model for the CuCl Z_1 and Z_3 transverse exciton bands. These models must of necessity (due to the number of propagating modes, i.e., spatial dispersion) combine Maxwell's boundary conditions with additional boundary conditions (ABCs). There are various possible ABCs reported in the literature, but the "Pekar ABC" has proved adequate for modeling our spectra. This ABC specifies that the total polarization due to each exciton branch disappears at the crystal interface or at a finite distance from the interface (in the latter case giving rise to an exciton dead layer (DL) as detailed elsewhere).[12]

Exciton-polariton mixed excitation modes are present within the crystal due to the coupling of the photon and free exciton modes. This coupling is strongest at the crossing points of these modes in the ω-k diagram and leads to a characteristic "anti-crossing" behaviour at such points which affects the refractive index close to the exciton energy regions and can thus be probed by reflection. For the case of a single exciton band, the coupling leads to two exciton-polariton modes propagating within the material, which in turn means three boundary conditions are needed, to describe the relative field strengths of the incoming and outgoing electromagnetic wave and the two propagating modes, as shown in Figure 1(a). Maxwell's equations give two boundary conditions (on the electric and magnetic fields) so another condition is needed. Pekar ABCs are used for this,

[a)]E-mail: barry.foy2@mail.dcu.ie.
[b)]E-mail: enda.mcglynn@dcu.ie.

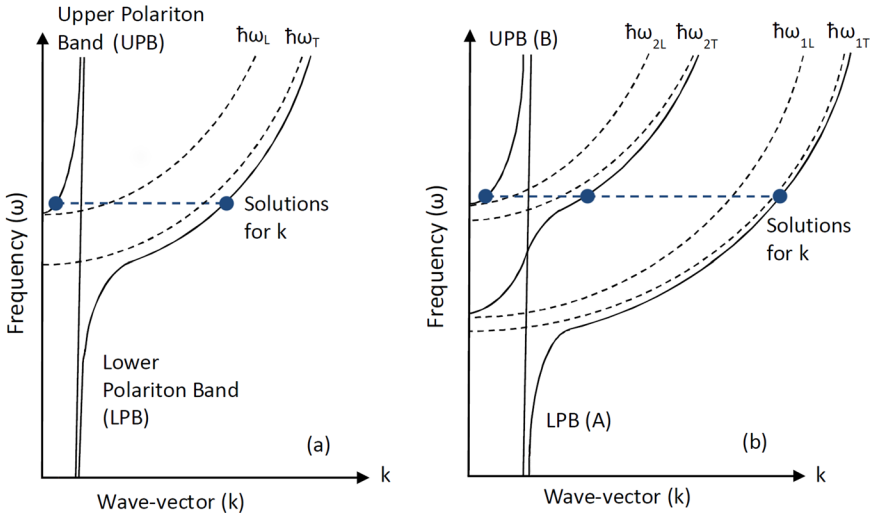

FIG. 1. (a) Schematic illustration of the mode frequency versus the positive real part of the wavevector for longitudinal and transverse exciton-polariton modes for a single exciton band scenario. The curved solid lines represent the dispersion relations of the coupled exciton-polariton modes, the nearly vertical straight solid line the uncoupled photon mode, and the dashed lines those of the uncoupled longitudinal and transverse exciton waves. As shown, a single exciton band leads to two propagating exciton-polariton modes. For lower frequencies and in the absence of damping, one mode has a purely real wavevector and the other a purely imaginary wavevector. (b) A similar schematic illustration for the case of two exciton bands (appropriate for CuCl) which now shows three propagating exciton-polariton modes. In both cases, an ABC is required when calculating reflectance data.

which require that the material polarization due to a particular exciton band vanish at a certain location in the crystal, usually at the surface or close to the surface, with the physical meaning that the exciton cannot leave the material. For material with two closely spaced exciton bands, such as the Z_3 and $Z_{1,2}$ exciton bands in CuCl, the situation is more complex. Three propagating exciton-polariton modes are present, with four boundary conditions required as shown in Figure 1(b). Two Pekar ABCs are used for both excitonic material polarizations.

Four different models are examined in our analysis. Model 1 applies Pekar's ABC at the air-CuCl interface and presumes a sample of bulk CuCl, treating the CuCl layer as semi-infinite. However, we expect the classical reflection point of the excitons to lie at a point deeper within the material, due to image charge and other surface effects.[10] To account for this, we have used the infinite-barrier approximation of Hopfield and Thomas in model 2 (and also model 4, see below) which effectively creates an exciton DL by simulating an infinite potential barrier through which the excitons cannot penetrate at a finite distance from the crystal interface. Therefore, model 2 applies the same ABC properties only at the air-CuCl interface as per model 1 and includes the DL thickness at the air-CuCl interface as a fitting parameter, applying Pekar's ABC at the DL boundary. Model 3 applies the same ABC properties at the air-CuCl interface and includes for the effects of the thickness of the thin film layer and reflections at the Si substrate. Model 4 is similar to model 3 considering the thin film to have a defined thickness with the addition of DLs at the air-CuCl and CuCl-Si boundaries.

Although we have chosen to use Pekar's ABCs, the simultaneous equations detailed below can be readily modified for other ABCs. The modeling algorithm calculates the reflection coefficient as a function of photon energy and enables determination of the relative electric field strengths due to different photon and polariton modes in various regions of the structure. Fabry-Perot effects[13] in our thin film samples are quite prominent and must be considered to accurately model the experimental data, especially in spectral regions away from exciton peak positions. The effect of the DLs at the film interface is shown to be minimal (due to the small excitonic Bohr radius and correspondingly small DL thickness and the larger surface roughness of our samples which will tend to average out any effects). Each of the models yield material parameter values in good agreement with previously reported literature values for bulk material and with independently verified parameters such as the measured thickness of the CuCl thin film.

II. EXPERIMENTAL TECHNIQUES

CuCl thin films are grown on (100) Si wafer substrates pieces approximately 2 cm by 1.5 cm in size, cut from a 4 in. wafer. These wafers are single-sided, polished, p-type boron-doped Si with a resistivity of $<20\ \Omega$cm. Prior to deposition, the substrates were degreased using Decon solution and organic solvents. The Si substrate native oxide is removed using dilute HF. Commercially available CuCl beads with 99.99% purity (Sigma-Aldrich) were evaporated from a quartz crucible onto the substrates using an Auto 306 Edwards evaporation system. The vacuum deposition was performed at $\sim 1 \times 10^{-6}$ mbar at a rate of ~ 0.5 nms^{-1} as measured by a quartz crystal oscillator and the nominal thickness of all samples studied was 500 nm. The actual thickness was found to be consistently higher than the nominal thickness and this is discussed more fully in Sec. IV. Upon completion of the deposition, it was essential that the samples were stored in a vacuum container at all times due to the hygroscopic nature of CuCl. Exposure to atmospheric moisture in air causes the optical properties of the material to rapidly decay due to an increase in the level of hydrated oxyhalides of Cu^{++}.[14] X-ray diffraction and scanning electron microscopy data (as shown in Figure 4(b) below) indicate that these films are nanocrystalline and textured with the CuCl [111] direction normal to the substrate surface, with a grain size of less than 50 nm estimated from scanning electron microscopy (SEM).

The low temperature reflectance spectra were acquired in a Janis CCS-500 closed-cycle cryostat in a He exchange gas environment at a temperature of 20 K. The temperature was controlled using an Oxford Instruments ITC-4 controller, resistive heater, and a 27 Ω rhodium-iron resistance

sensor on the sample holder. A deuterium lamp illuminated the samples during reflectance scans and the angle of incidence was $<10°$ relative to the normal to the sample surface. Spectra were acquired using a Bomem DA8 Fourier Transform spectrometer fitted with a Hamamatsu R1913 photomultiplier (PM) tube with the PM output matched to the spectrometer using a Bomem variable gain preamplifier. The resolution of the spectra acquired using this setup is ~0.1 meV. An Al-coated Si sample was used as a reflectance reference to ensure the calculated reflectance is for the CuCl thin film rather than any other factors. This was deposited onto the Si using the same setup as the CuCl deposition. SEM scans were performed at room temperature using a LEO Stereoscan 440 SEM. The samples were excited with the electron beam set to <15 keV (chosen depending on the sample details) and a probe current of typically 0.1 nA. More detail on the experimental set-up is given in Refs. 15 and 16.

III. REFLECTANCE MODELING

The total electrical polarizability within a medium can be split into three distinct parts, the electronic, ionic, and dipolar. Electronic polarizability occurs within the high-frequency optical and near-UV regions of the reflectance spectra which is the region of interest for the CuCl exciton spectra. The contribution of the excitons to the polarizability is accounted for by expressing the total excitonic polarizability as a sum of each of the contributing excitonic bands (represented by j) for a given wave vector k and frequency ω

$$\alpha(\omega,k)=\sum\nolimits_j \frac{\alpha_{0j}\omega_{jT}^2}{\omega_{jT}^2-\omega^2+\beta_j k^2-i\omega\Gamma_j}, \tag{1}$$

where α_{0j} are the polarizabilities of each exciton resonance j at $\omega=0$ and $k=0$, ω_{jT} are the transverse excitonic resonance frequencies at $k=0$ for the jth exciton band, and Γ_j is the empirical damping coefficients for the jth exciton band. The influence of spatial dispersion is described by

$$\beta_j k^2=\left(\frac{\hbar\omega_{jT}}{M_j}\right)k^2, \tag{2}$$

where M_j is the effective exciton mass and $\hbar$ is Planck's constant divided by 2π.

The frequencies under examination in this paper occur near two exciton resonances in CuCl, i.e., the Z_3 and $Z_{1,2}$ free exciton bands (hereafter called A and B, respectively). The total polarizability at these frequencies is the sum of these excitonic oscillators and a wave-vector independent background polarizability α_∞

$$\alpha(\omega,k)=\alpha_\infty+\frac{\alpha_{0A}\omega_{AT}^2}{\omega_{AT}^2-\omega^2+\beta_A k^2-i\omega\Gamma_A}+\frac{\alpha_{0A}\omega_{BT}^2}{\omega_{BT}^2-\omega^2+\beta_B k^2-i\omega\Gamma_B}. \tag{3}$$

The relation $\varepsilon\varepsilon_0E=\varepsilon_0E+\alpha E$ between the electric field E in the crystal, the permittivity of the vacuum ε_0, the polarizability α, and the dielectric function ε leads to an expression for the permittivity of the material at such frequencies as follows:

$$\varepsilon(\omega,k)=\varepsilon_\infty+\frac{\alpha_{0A}}{\varepsilon_0}\frac{\omega_{AT}^2}{\omega_{AT}^2-\omega^2+\beta_A k^2-i\omega\Gamma_A}+\frac{\alpha_{0B}}{\varepsilon_0}\frac{\omega_{BT}^2}{\omega_{BT}^2-\omega^2+\beta_B k^2-i\omega\Gamma_B}, \tag{4}$$

where ε_∞ is a frequency and wave-vector independent background dielectric constant ($\varepsilon\to\varepsilon_0$ as $\omega\to\infty$). The value of ε_∞ used in this work is 3.7, based on previous work.[7] The transverse solutions of Maxwell's equation (assuming the magnetic permeability of the crystal is that of free space, i.e., the relative permeability $\mu_r=1$) are given by the condition that

$$\varepsilon(\omega,k)=\frac{k^2c^2}{\omega^2}. \tag{5}$$

Substituting Eq. (4) for the dielectric constant into Eq. (5), the condition for transverse solutions for two excitonic bands becomes

$$\frac{k^2c^2}{\omega^2}=\varepsilon_\infty+\frac{\alpha_{0A}}{\varepsilon_0}\left(\frac{\omega_{AT}^2}{\omega_{AT}^2+\beta_A k^2-\omega^2-i\omega\Gamma_A}\right)+\frac{\alpha_{0B}}{\varepsilon_0}\left(\frac{\omega_{BT}^2}{\omega_{BT}^2+\beta_B k^2-\omega^2-i\omega\Gamma_B}\right). \tag{6}$$

There are two frequencies ω for which the value of the dielectric constant (the r.h.s. of Eq. (6)) will become zero at each value of k and these correspond to the longitudinal polariton bands of both the A and B excitons, as shown in Figure 1. The values of these frequencies at k = 0 yield the so-called longitudinal frequencies (also called the longitudinal resonance frequencies in Ref. 17) of the two longitudinal polariton bands, ω_{AL} and ω_{BL}, respectively. The difference between these longitudinal frequencies and the transverse excitonic resonance frequencies mentioned above are related to the polarizabilities of the exciton resonances and these longitudinal-transverse (LT) splittings are normally used as the variable to express the degree of exciton-photon coupling for each resonance and are the quantities we use when reporting and discussing results below. The two are related via an argument which ultimately leads to a modified Lyddane-Sachs-Teller relation[17] and the necessary relations to convert between the two are as follows:

$$\alpha_{A0}=\varepsilon_\infty\left(\frac{\varepsilon_0}{\omega_{AT}^2}\right)(\omega_{BL}^2-\omega_{AT}^2)\left(\frac{\omega_{AL}^2-\omega_{AT}^2}{\omega_{BT}^2-\omega_{AT}^2}\right) \tag{7}$$

and

$$\alpha_{B0}=\varepsilon_\infty\left(\frac{\varepsilon_0}{\omega_{BT}^2}\right)(\omega_{AL}^2-\omega_{BT}^2)\left(\frac{\omega_{BL}^2-\omega_{BT}^2}{\omega_{AT}^2-\omega_{BT}^2}\right). \tag{8}$$

In our analysis, we only consider transverse modes because these are the only modes coupled to by incident radiation

impinging at normal angles of incidence, as stated previously.[10] The β parameters may be different for both the A and B excitons because these are related to the transverse frequency and the effective mass of the individual exciton. To simplify Eq. (6), we may express it as

$$Ak^2 = \varepsilon_\infty + \frac{B}{C + \beta_A k^2} + \frac{D}{E + \beta_B k^2}, \tag{9}$$

where we have the following identifications:

$$A = \frac{c^2}{\omega^2}, \quad B = \frac{\alpha_{A0}}{\varepsilon_0}\omega_{AT}^2, \quad C = \frac{\varepsilon_0 B}{\alpha_{A0}} - \omega^2 - i\omega\Gamma_A,$$
$$D = \frac{\alpha_{B0}}{\varepsilon_0}\omega_{BT}^2, \quad E = \frac{\varepsilon_0 D}{\alpha_{B0}} - \omega^2 - i\omega\Gamma_B. \tag{10}$$

Multiplying by the denominators on the right-hand side of Eq. (9) leads to

$$Ak^2(C + \beta_A k^2)(E + \beta_B k^2) = \varepsilon_\infty(C + \beta_A k^2)(E + \beta_B k^2) + B(E + \beta_B k^2) + D(C + \beta_A k^2), \tag{11}$$

and after multiplying the out the bracketed parameters and collecting terms of similar order in k, one obtains the expression

$$(A\beta_A\beta_B)k^6 + (AC\beta_B + AE\beta_B - \varepsilon_\infty\beta_A\beta_B)k^4 + (ACE - \varepsilon_\infty C\beta_B - \varepsilon_\infty C\beta_A - B\beta - D\beta)k^2 - (\varepsilon_\infty CE + BE + DC) = 0. \tag{12}$$

This, when re-arranged, leads to an equation cubic in k^2 for each value of ω, and thus for each optical frequency, there are 3 different modes, with three different k values, which we denote by subscripts (k_i). These k values may be complex and the sign of the k value used (i.e., the positive or negative solution of $\sqrt{k^2}$) is chosen to conform with physically meaningful boundary conditions (e.g., a solution vanishing far from a boundary or the correct direction of energy transfer). Each of these propagating modes has an associated refractive index, n_i, at each value of ω, given by $n_i = \omega/k_i$. These refractive indices form the basis for modeling the reflectance spectra.

To solve for the reflectance and transmission of propagating modes at interfaces at optical frequencies, we need to use a matrix approach. In doing so, we have modeled four of the different scenarios possible using different combinations of DLs as well as treating the thin layer sample as a bulk sample before including the thickness of the material, as described previously and as shown in Figure 2. The relevant equations and theory behind each of these matrix models will now be discussed. Since each of the models has a similar underlying structure, they will be described in order of complexity with each model building upon the previous.

A. Model 1 (air–bulk CuCl)

This basic model considers the incident and reflected rays (E_I and E_R, respectively) in air (with refractive index n_0, taken equal to 1), and the three exciton-polariton modes predicted by Eq. (6) (E_{1-3}), where the refractive index is n_{1-3} for each corresponding mode. The CuCl layer is assumed to be semi-infinite and all other factors such as the CuCl/Si interface and excitonic DLs are omitted, so that only right propagating exciton polariton modes are considered, as shown in Figure 2(a). When Maxwell's equations are

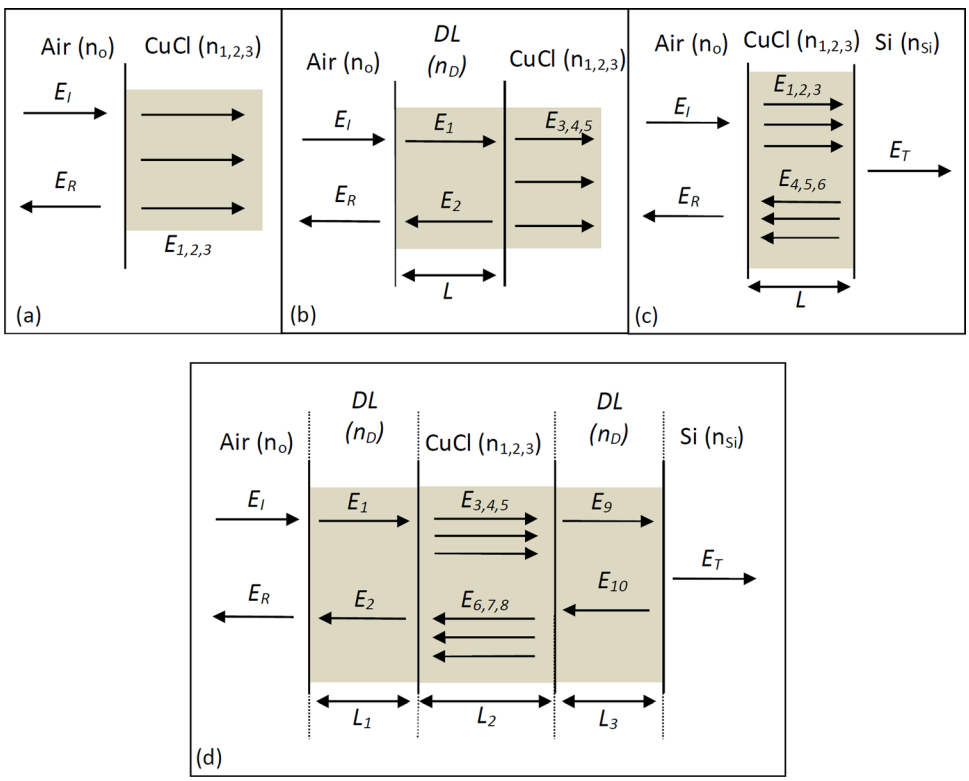

FIG. 2. Photon and exciton-polariton modes for (a) model 1 (b) model 2 (c) model 3, and (d) model 4. Electric field amplitudes are labelled E_i. Layer thicknesses are labelled L_i and refractive indices as n_i.

combined with the ABC Pekar boundary conditions, the following set of simultaneous equations is obtained for the boundary conditions:

$$E_1 + E_R = E_1 + E_2 + E_3, \tag{13}$$

$$n_0 E_1 - n_0 E_R = n_1 E_1 + n_2 E_2 + n_3 E_3, \tag{14}$$

$$\alpha_A(k_1, \omega)E_1 + \alpha_A(k_2, \omega)E_2 + \alpha_A(k_3, \omega)E_3 = 0, \tag{15}$$

$$\alpha_B(k_1, \omega)E_1 + \alpha_B(k_2, \omega)E_2 + \alpha_B(k_3, \omega)E_3 = 0, \tag{16}$$

where n_i represents the refractive index n_1, n_2, and n_3 and $\alpha(k_i,\omega)$ is the polarizability of the A or B free excitons as a function of frequency for each of the three solutions for the wavevector $k_{1,2,3}$, i.e., at the values of ω and three k values ($k_{1,2,3}$) which result from solving Eqs. (6)–(12). Equations (13) and (14) above correspond to the boundary conditions from Maxwell's equations and Eqs. (15) and (16) to the Pekar ABCs for the A and B exciton bands, respectively, showing that the total material polarization due to each exciton band (itself caused by the electric fields of the associated propagating exciton-polariton mode) vanishes, in this case at the surface. Equation (13) is represented visually in Figure 2(a). The contribution of the polarizability $\alpha(k_i,\omega)$ for each exciton band is as previously defined in Eq. (3). The boundary conditions above can then be expressed in the matrix form:

$$\begin{pmatrix} -1 & 1 & 1 & 1 \\ 1 & n_1 & n_2 & n_3 \\ 0 & \alpha_{A1} & \alpha_{A2} & \alpha_{A3} \\ 0 & \alpha_{B1} & \alpha_{B2} & \alpha_{B3} \end{pmatrix} \begin{pmatrix} r \\ A \\ B \\ C \end{pmatrix} = \begin{pmatrix} 1 \\ 1 \\ 0 \\ 0 \end{pmatrix}, \tag{17}$$

where the relative field intensities are defined as follows: $r = E_R/E_I$, $A = E_1/E_I$, $B = E_2/E_I$, and $C = E_3/E_I$. $\alpha_{A1\text{-}3}$ are the frequency dependent polarizabilities defined in Eq. (17) for the A free excitons with wavevectors k_{1-3} and $\alpha_{B1\text{-}3}$ are the corresponding frequency dependent polarizabilities for the B free excitons with wavevectors k_{1-3}. The refractive index of air has been set to unity for this model and throughout the rest of the analysis. n_{1-3} represents the refractive index for each of the E_{1-3} modes. The matrix above takes the form $Xy = z$. This implies that, by taking the inverse of the square matrix X, we can solve for the column vector y, whose first element is the reflection coefficient r, i.e., $y = X^{-1}z$ so *y(1)* gives us r. Squaring this gives us the reflectance R. The A, B, and C values (i.e., *y(2)*, *y(3)*, and *y(4)*) provide the relative interface field amplitudes and phases (because these are complex numbers) for the propagating polariton modes within the structure. These and later matrix operations were performed using MATLAB.

B. Model 2 (air–DL–CuCl)

For this model shown in Figure 2(b), we apply an additional DL to the theory of model 1. The thickness of this layer is denoted by the fitting parameter L resulting in the following matrix equation, derived similarly to the case for model 1, using the various propagating modes shown in the figure:

$$\begin{pmatrix} r \\ A \\ B \\ C \\ D \\ E \end{pmatrix} = \begin{pmatrix} -1 & 1 & 1 & 0 & 0 & 0 \\ 1 & n_D & -n_D & 0 & 0 & 0 \\ 0 & e & e_* & -1 & -1 & -1 \\ 0 & n_D e & -n_D e_* & -n_1 & -n_2 & -n_3 \\ 0 & 0 & 0 & \alpha_{A1} & \alpha_{A2} & \alpha_{A3} \\ 0 & 0 & 0 & \alpha_{B1} & \alpha_{B2} & \alpha_{B3} \end{pmatrix}^{-1} \begin{pmatrix} 1 \\ 1 \\ 0 \\ 0 \\ 0 \\ 0 \end{pmatrix}, \tag{18}$$

where e represents $exp\left(i\frac{n_D \omega L}{c}\right)$ and e_* represents $exp\left(-i\frac{n_D \omega L}{c}\right)$, i.e., the phase shifts for photon modes propagating back and forth in the DL. n_D represents the DL refractive index defined as $n_D = \sqrt{\varepsilon_\infty}$. The equation is solved for r and r is then squared to obtain the reflectance.

C. Model 3 (air–CuCl–Si)

For the third model, shown in Figure 2(c), each of the parameters of the first model are included with an accommodation of the thin film nature of the sample and reflection from the CuCl/Si interface. The thickness is denoted by L and used as an additional fitting parameter. These additional parameters require the use of further boundary conditions. These are applied at each of the interfaces and state that the polarization due to the excitons must be zero at the air-CuCl and CuCl-Si interfaces as we are not taking the DLs into account in this model. The two resonances obtained for the A and B excitons at the air-CuCl interface are

$$\alpha_{0A}(k_1,\omega)[E_1+E_4]+\alpha_{0A}(k_2,\omega)[E_2+E_5]+\alpha_{0A}(k_3,\omega)[E_3+E_6]=0, \tag{19}$$

with α_{0A} representing the polarizability factor for the *A* exciton and, *mutatis mutandis*, α_{0B} for the *B* exciton resonance equation

$$\alpha_{0B}(k_1,\omega)[E_1+E_4]+\alpha_{0B}(k_2,\omega)[E_2+E_5]+\alpha_{0}(k_3,\omega)[E_3+E_6]=0. \tag{20}$$

Similarly at the CuCl-Si interface, the additional boundary conditions obtained are

$$\alpha_{0A}(k_1,\omega)[E_1e^{i(n_1\omega^L/c)}+E_4e^{-i(n_1\omega^L/c)}]+\alpha_{0A}(k_1,\omega)[E_2e^{i(n_2\omega^L/c)}+E_5e^{-i(n_2\omega^L/c)}]+\alpha_{0A}(k_1,\omega)[E_3e^{i(n_3\omega^L/c)}+E_6e^{-i(n_3\omega^L/c)}]=0 \tag{21}$$

for the A exciton. The additional B exciton boundary conditions are similar and given by

$$\alpha_{0B}(k_1,\omega)[E_1e^{i(n_1\omega^L/c)}+E_4e^{-i(n_1\omega^L/c)}]+\alpha_{0B}(k_1,\omega)[E_2e^{i(n_2\omega^L/c)}+E_5e^{-i(n_2\omega^L/c)}]+\alpha_{0B}(k_1,\omega)[E_3e^{i(n_3\omega^L/c)}+E_6e^{-i(n_3\omega^L/c)}]=0. \tag{22}$$

The additional *E* values are added to our existing boundary conditions given in Eqs. (13)–(16) and expressed in matrix form. The solution is

$$\begin{pmatrix} r\\A\\B\\C\\D\\E\\F\\G\end{pmatrix}=\begin{pmatrix} -1 & 1 & 1 & 1 & 1 & 1 & 1 & 0\\ 1 & n_1 & n_2 & n_3 & -n_1 & -n_2 & -n_3 & 0\\ 0 & e_1 & e_2 & e_3 & e_{*1} & e_{*2} & e_{*3} & -1\\ 0 & n_1e_1 & n_2e_2 & n_3e_3 & -n_1e_{*1} & -n_1e_{*2} & -n_1e_{*3} & -n_{Si}\\ 0 & \alpha_{A1} & \alpha_{A2} & \alpha_{A3} & \alpha_{A1} & \alpha_{A2} & \alpha_{A3} & 0\\ 0 & \alpha_{B1} & \alpha_{B2} & \alpha_{B3} & \alpha_{B1} & \alpha_{B2} & \alpha_{B3} & 0\\ 0 & \alpha_{A1}e_1 & \alpha_{A2}e_2 & \alpha_{A3}e_3 & \alpha_{A1}e_{*1} & \alpha_{A2}e_{*2} & \alpha_{A3}e_{*3} & 0\\ 0 & \alpha_{B1}e_1 & \alpha_{B2}e_2 & \alpha_{B3}e_3 & \alpha_{B1}e_{*1} & \alpha_{B2}e_{*2} & \alpha_{B3}e_{*3} & 0\end{pmatrix}^{-1}\begin{pmatrix}1\\1\\0\\0\\0\\0\\0\\0\end{pmatrix}, \tag{23}$$

where $e_i=exp\left(i\frac{n_i\omega L}{c}\right)$ and $e_{*i}=exp\left(-i\frac{n_i\omega L}{c}\right)$, i.e., the phase shifts for exciton-polariton modes propagating back and forth in the film layer and n_{Si} represents the refractive index of silicon which at 3.2 eV is ~5.5.[18] As before, this equation is solved for the amplitude reflection coefficient r which is then squared to obtain the reflectance.

D. Model 4 (air–DL–CuCl–DL–Si)

For the fourth model shown in Figure 2(d), we include the addition of exciton DLs at the air/CuCl and CuCl/Si interfaces to the thin film character of the third model. Each of these DLs have associated fitting parameters L_1 and L_3, respectively, with the thickness of the CuCl layer represented by L_2. The boundary conditions of the DLs are included in a manner similar to that used previously and the previous matrix is augmented and rearranged to give

$$\begin{pmatrix} r\\A\\B\\C\\D\\E\\F\\G\\H\\I\\J\\K\end{pmatrix}=\begin{pmatrix} -1 & 1 & 1 & 0 & 0 & 0 & 0 & 0 & 0 & 0 & 0 & 0\\ 1 & n_D & -n_D & 0 & 0 & 0 & 0 & 0 & 0 & 0 & 0 & 0\\ 0 & -e_{D1} & -e_{*D1} & 1 & 1 & 1 & 1 & 1 & 1 & 0 & 0 & 0\\ 0 & -n_De_{D1} & n_De_{*D1} & n_1 & n_2 & n_3 & n_1 & n_2 & n_3 & 0 & 0 & 0\\ 0 & 0 & 0 & e_{12} & e_{22} & e_{32} & e_{*12} & e_{*22} & e_{*32} & -1 & -1 & 0\\ 0 & 0 & 0 & n_1e_{12} & n_2e_{22} & n_3e_{32} & n_1e_{*12} & n_2e_{*22} & n_3e_{*32} & -n_D & n_D & 0\\ 0 & 0 & 0 & 0 & 0 & 0 & 0 & 0 & 0 & e_{D3} & e_{*D3} & -1\\ 0 & 0 & 0 & 0 & 0 & 0 & 0 & 0 & 0 & n_De_{D3} & -n_De_{*D3} & -n_{Si}\\ 0 & 0 & 0 & \alpha_{A1} & \alpha_{A2} & \alpha_{A3} & \alpha_{A1} & \alpha_{A2} & \alpha_{A3} & 0 & 0 & 0\\ 0 & 0 & 0 & \alpha_{B1} & \alpha_{B2} & \alpha_{B3} & \alpha_{B1} & \alpha_{B2} & \alpha_{B3} & 0 & 0 & 0\\ 0 & 0 & 0 & \alpha_{A1}e_{12} & \alpha_{A2}e_{22} & \alpha_{A3}e_{32} & \alpha_{A1}e_{12} & \alpha_{A2}e_{22} & \alpha_{A3}e_{32} & 0 & 0 & 0\\ 0 & 0 & 0 & \alpha_{B1}e_{12} & \alpha_{B2}e_{22} & \alpha_{B3}e_{32} & \alpha_{B1}e_{12} & \alpha_{B2}e_{22} & \alpha_{B3}e_{32} & 0 & 0 & 0\end{pmatrix}\begin{pmatrix}1\\1\\0\\0\\0\\0\\0\\0\\0\\0\\0\\0\end{pmatrix}, \tag{24}$$

where e_{ij} represents $exp(i\frac{n_i\omega L_j}{c})$ with n_i representing the refractive indices as in previous models, and $n_D = \sqrt{\varepsilon_\infty}$ now also included for the DLs. L_j represents the lengths L_1, L_3, and L_2 for the two DLs at each of the interfaces and the CuCl thin layer thickness, respectively. Similar to model 2, e_{*ij} represents $exp(-i\frac{n_i\omega L_j}{c})$ As in each of the previous models, the equation is solved for the amplitude coefficient r and squared to give the reflectance.

IV. MODELING RESULTS

The fitting is an iterative and self-consistent procedure, but in order to to ensure convergence within reasonable timescales, initial value estimates are taken from the experimental data for the transverse and longitudinal frequencies (because the longitudinal-transverse splitting is related to the polarizability of each exciton resonance, α_0 (Ref. 10)) of the excitons *A* and *B* which can be estimated from the maximum and minimum reflectivity energy positions at the exciton resonance region.[10] The static background dielectric constant, ε_∞, can be estimated from the average reflection coefficient sufficiently far below the excitonic resonance. By varying parameters such as the *A* and *B* longitudinal and transverse exciton energies, the damping coefficients, exciton masses, CuCl thin film thickness (for models 3 and 4) and in the case of models 2 and 4, the DL thicknesses, reflectance spectra are produced which are then optimized in terms of similarity to the experimental data using a least squares fitting procedure in MATLAB.

Figure 3 shows the experimental reflectance data plotted alongside the best fits for each of the models used to fit that data. We can see that each of the models quite closely matches the experimental data for the Z_3 exciton with models 3 and 4 being slightly closer to the measured experimental values for the Z_3 exciton (3.202 eV) and the $Z_{1,2}$ exciton (3.272 eV). These two models are practically identical, indicating the very small influence of the DL on the fitted reflectance data. The Fabry-Perot oscillations visible are present throughout the experimental spectra and spectra incorporating the CuCl thin film nature at spectral regions away from the exciton positions. The calculated exciton-polariton dispersion curves for CuCl from our analysis closely matches that reported in previous work which also calculated the three-branch CuCl exciton-polariton dispersion curve using a two-oscillator model.[19]

Fabry-Perot oscillations will be observed only when the spatial damping of the propagating modes is sufficiently small that at least some of the modes can make at least two passes through the sample. This requires the sample thickness to be significantly less than *L*, the damped path length of an exciton polariton mode, where $L = (n_i\, k_0)^{-1}$, n_i is the imaginary part of the mode refractive index and k_0 is the free space wavevector.[20] In the regions close to the exciton resonance energy positions, the value of *L* will be decreased significantly due to the strong mixture of more heavily damped exciton-like character in all propagating modes and thus no fringes should be visible at these positions. At photon energies below and between the exciton resonance energy positions, the *L* value for photon-like modes (with a small exciton-like character) will greatly increase and these fringes will become prominent, as has been reported previously for ZnO thin films.[15,16] This trend is clearly shown in Figure 3, with the Fabry-Perot fringes increasing in prominence below and between the exciton resonance energy positions.

Fringes are not seen at higher photon energies, possibly due to the effects of the onset of direct optical transitions in Si at energies of ~3.3 eV, which affect the Si refractive

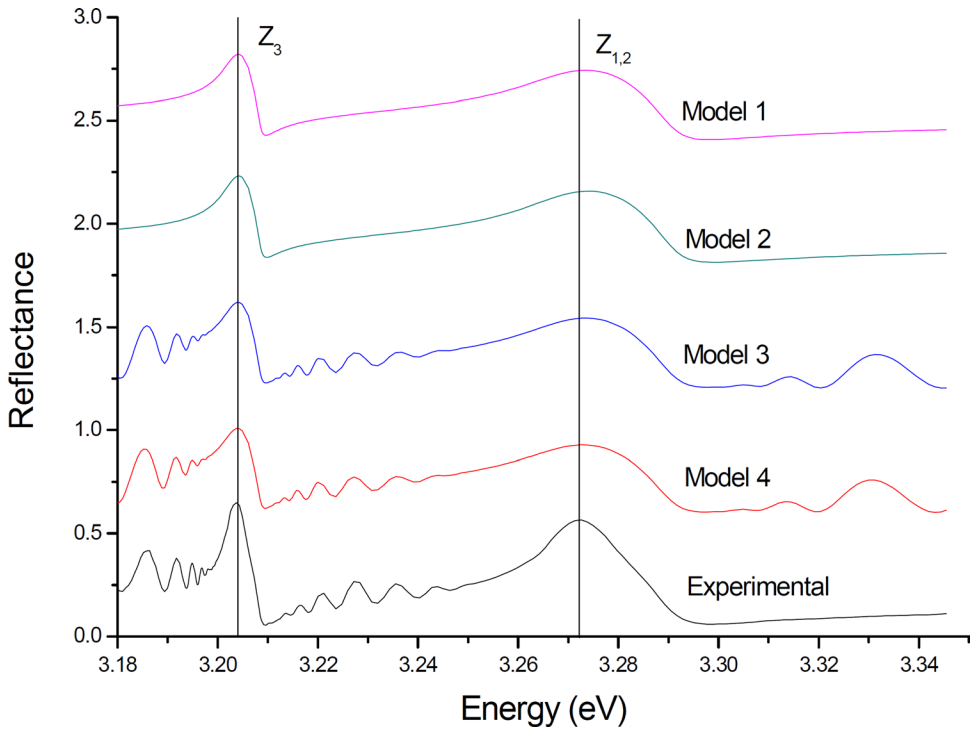

FIG. 3. Experimental and best fit modeled reflectance spectra plotted for each of the reflectance models 1–4 described in the text. Each spectrum has been offset on the intensity axis from its neighbours by 0.6 for clarity. The CuCl thin film experimental data are shown at its recorded reflectance values. The details of the layer structures of each model are as follows: model 1: Air–Bulk CuCl; model 2: Air–DL–Bulk CuCl; model 3: Air–Thin film CuCl–Si substrate; model 4: Air–DL–Thin film CuCl–DL–Si substrate.

index values in that spectral region (and these values will then differ from the value of ~5.5 used in our model and fitting procedure) and will alter the reflection coefficient at the CuCl-Si interface in a way that is not well reproduced by our model.[21]

Table I shows the best-fit values to our data, determined using model 3, alongside previously reported values for bulk CuCl.[7] Both our modeled spectra and the referenced bulk sample have used a value of 3.7 for ε_∞. The number of significant figures for modeled parameters were chosen to match those from Ref. 7 for the same parameters to enable comparisons. The number of significant figures for the film thickness was taken as 3 (i.e., approximately ± 10 nm) which is the estimated error on actual film thickness measurements from SEM data. Little variation was found across the models for each of the parameters with the exciton peak positions remaining somewhat constant with the accuracy of the shape of the Fabry-Perot fringes providing the only significant differences. The majority of the material's values closely match the bulk samples except for the effective masses of each of the excitons and the damping coefficient of the $Z_{1,2}$ exciton. The effect of effective masses on the shape of the modeled spectra is mainly seen in the relative intensity and shape of the exciton peaks; specifically the higher this value, the smaller and more asymmetric these peaks will become. Slight systematic errors in the overall reflectance values possibly due to the nature of the reflectance reference are therefore likely to be the origin of some of this discrepancy. From observation of our best fit spectra, there is also a slight difference in the peak shape, with our modeled spectra being slightly more rounded than the experimental peaks, suggesting that a larger exciton mass is required, in line with the discrepancy with respect to previously reported values. However, practical limitations in terms of the MATLAB model become important in this regard. The limits of MATLAB in terms of floating point numbers are ±1.7977e+308. As the thickness of the thin film is increased, the arguments of the e_1 and e_2 parameters present in each of the matrices used in models 3 and 4 tends to increase above this limit at lower frequency values and thus produce another systematic error likely to contribute to the observed discrepancy in exciton effective masses. Artificially decreasing the exciton masses keeps the arguments within the programming limitations but results in slight inaccuracies in the exciton mass values. However, this decrease allows us to model the Fabry-Perot fringes at lower energy values and allows us to ensure the thickness value results in accurate fringe production in the spectral region between the two exciton peaks visible in Figure 3.

For the case of the $Z_{1,2}$ exciton damping coefficient, we note that there may also be some interplay in the fitting procedure between the exciton masses and the damping coefficients, especially in the case of the larger damping coefficient for the $Z_{1,2}$ exciton, which would account for this latter discrepancy. The most notable point in terms of the damping coefficients for both excitons, however, is that they are of the same order of magnitude as those of the bulk crystal, unlike the case of ZnO thin films where the thin film damping coefficients are an order of magnitude larger than those of the bulk ZnO crystal.[15,16] This is due to the much larger excitonic binding energies in CuCl compared to ZnO (190 meV versus 60 meV) which means the excitonic complex in CuCl is much more stable in a poorer quality nanocrystalline thin film environment.

The best fit film thickness is found to be ~1000 nm and this is larger than the nominal deposited 500 nm thin film thickness of the CuCl samples. However, a number of factors can serve to increase the actual thickness above the 500 nm nominal thickness, including the position of the Si substrates in relation to the evaporation crucible, orientation of the shielding plate to restrict deposition until an ideal rate has been reached, and the general non-uniformity of the surface of these samples. All these factors likely contribute to an increase of the actual CuCl thickness over the nominal value. SEM measurements performed in cross-sectional geometry on a CuCl thin film on Si revealed the actual layer thickness to be ~1080 nm, even though the nominal deposition thickness was 500 nm, thus validating the accuracy of the fitted

TABLE I. Fitting parameters used for modeling the CuCl thin film sample using model 3 and data for bulk CuCl from the literature for comparison.

Parameter	Bulk CuCl (Ref. 7)	Sample 1	Sample 2	Sample 3
$\hbar\varpi_{AT}$ (transverse Z_3 exciton energy, eV)	3.202	3.203	3.203	3.202
$\hbar\varpi_{BT}$ ($Z_{1,2}$ transverse exciton energy)	3.266	3.267	3.267	3.266
$\hbar\varpi_{AT} - \hbar\varpi_{BT}$ (Z_3-$Z_{1,2}$ splitting, meV)	64	64	64	64
Δ_{LT}^{A} (Z_3 exciton LT splitting, meV)	5.7	5.8	4.5	5.4
Δ_{LT}^{B} ($Z_{1,2}$ exciton LT splitting, meV)	23	23.5	19	23
$\hbar\Gamma_A$ (Z_3 exciton damping, meV)	0.9	1.6	1.1	1.1
$\hbar\Gamma_B$ ($Z_{1,2}$ exciton damping, meV)	11.5	8.6	9.9	5.8
M_A (multiples of electron mass for Z_3)	2.4	0.4	0.8	0.3
M_B (multiples of electron mass for $Z_{1,2}$)	0.65	0.08	0.15	0.06
DL thickness Z_3 exciton (nm)	1.4	0	0	0
DL thickness $Z_{1,2}$ exciton (nm)	2.8	0	0	0
Film thickness (nm) (All 500 nm nominal thickness)		Sample 1	Sample 2	Sample 3
Fitted	N/A	1000	750	690
Measured	N/A	1080	730	680

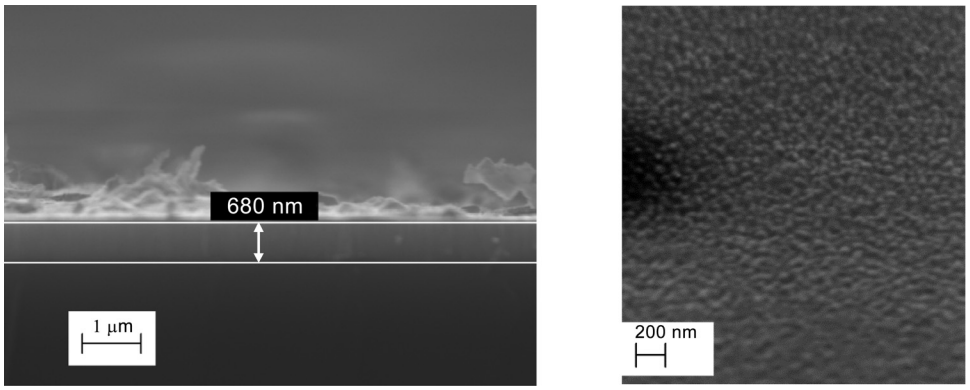

FIG. 4. (a) Cross-sectional of CuCl thin film sample showing the physical thickness. The white fiducial lines have been slightly shifted for clarity. The debris present on the CuCl surface is due to the cleaving process used to prepare samples for the cross-sectional SEM measurements and not representative of the CuCl sample surface. (b) Tilted SEM image of the surface taken at close to 30° of the CuCl thin film sample showing the surface roughness.

thickness value for other samples. Further reflectance measurements on samples of actual thicknesses ~680 nm and ~730 nm (as determined by cross-sectional SEM measurements with data shown in Figure 4(a) for the sample of actual thickness 680 nm) yielded best fit thicknesses of 690 nm and 750 nm, respectively, further validating the accuracy of the fitted film thickness parameter.

The critical dead layer thickness in bulk CuCl has previously been calculated to be ~1.4 and 2.8 nm for Z_3 and $Z_{1,2}$ excitons, respectively, and the authors say that above this value, the fit of the reflectance spectra is destroyed;[7] however, this was not the case in our model. Dead layer thicknesses below these values have no discernible effect on the modeled spectra, shown by models 2 and 4 in Figure 3. The dead layer value was set to these previously calculated values to try and show the effect of the layers and in model 4, a slight flattening of the Z_3 exciton peak can be observed while model 2 has no discernible differences. Increasing the dead layer value causes a decrease in the peak height at each of the exciton positions and a slight change in the location of the Fabry-Perot fringes.

The lower values used for the exciton effective masses already cause the peak heights to be decreased, so the model tends to reduce the dead layer thickness to 0 to maintain accuracy at these locations. Using either previously calculated or physically plausible values based on the excitonic radius for the DL thickness results in modeled spectra practically identical to ones in which the DL thickness is set to zero, i.e., model 1 being identical to model 2 and model 3 identical to model 4. The lack of effect of this dead layer is probably due to the excitonic radius for CuCl being 0.7 nm (Refs. 5 and 22) which is very small when compared to other copper halides. The influence of the DLs is essentially due to Fabry-Perot interferences in those layers, which become negligible for very thin layers.[7,10] Furthermore, in the present samples, the surface roughness is likely to be considerably greater than any physically plausible value of DL thickness and thus any such effects are likely to be further averaged out by the surface roughness in the experimental spectra as demonstrated by Figure 4(b).

The values previously reported for bulk CuCl are expected to correspond to an unstrained crystal. Any differences observed in either our data or fits could possibly be due to strain in the thin film. However, the good agreement of the fit values with the bulk values indicates a lack of significant strain in the CuCl thin film, because of the close lattice matching of CuCl to the Si substrate.[3] Minor discrepancies in the LT splitting and exciton damping coefficients occur for the $Z_{1,2}$ exciton peak, which is broader than the Z_3 peak, leading to slightly greater fitting errors.

V. CONCLUSIONS

We have used a two-band dielectric response function to model normal incidence reflectance spectra from thin film CuCl films on Si substrates. The models have been described in detail along with the boundary conditions and we have included the influence of finite film thickness and excitonic DLs, both of which may lead to spectral structure such as Fabry-Perot oscillations. The modeled spectra provide a very good fit to the experimental data in the spectral region of the excitonic peak structure and, when the thin film effects are included, also fit the Fabry-Perot oscillations at lower energies very well. The fitting parameters found using a least squares best fit optimization were compared to previously reported values for bulk CuCl samples and excellent agreement was found.

Thus our modeling analysis provides a sensitive and non-destructive means of determining both CuCl thin film free exciton-polariton properties and film thicknesses, and thus a method for studying influences which might perturb these properties (e.g., strain). For example, strain effects in thin films can significantly alter the exciton energies and bandgap values, as has been reported for ZnO thin films.[23] CuCl reflectance spectroscopy (conducted in a cryostat in a He atmosphere) is particularly well suited to studies of CuCl due to the hygroscopic nature of the material because one can control and indeed reduce/eliminate the normal atmospheric exposure-related decay of the samples even over the course of extended measurements.

ACKNOWLEDGMENTS

The authors gratefully acknowledge funding from Science Foundation Ireland under the Research Frontiers programme and Enterprise Ireland under the Proof of Concept programme.

[1]S. Nakamura, and G. Fasol, *The Blue Laser Diode: GaN Based Light Emitters and Lasers* (Springer, Berlin, 1997).
[2]O. Ambacher, J. Phys. D: Appl. Phys. **31**, 2653 (1998).
[3]N. Nishida, K. Saiki, and A. Koma, Surf. Sci. **324**, 149 (1995).

[4]T. Koda, T. Murahashi, T. Mitani, S. Sakoda, and Y. Onodera, Phys. Rev. B **5**, 705 (1972).
[5]Z. K. Tang, A. Yanase, T. Yasui, Y. Segawa, and K. Cho, Phys. Rev. Lett. **71**, 1431 (1993).
[6]A. Silva-Castillo and R. Perez-Rodriguez, J. Appl. Phys. **90**, 3662 (2001).
[7]M. Soltani, M. Certier, P. Becker, H. Aourag, and B. Khelifa, Comput. Mater. Sci. **4**, 263 (1995).
[8]G. Oohata, T. Nishioka, D. Kim, H. Ishihara, and M. Nakayama, in *8th International Conference on Excitonic Processes in Condensed Matter (EXCON 2008)*, edited by T. Itoh, K. Tanaka, and M. Schreiber (Wiley-VCH Verlag Gmbh, Kyoto, Japan, 2008), p. 280.
[9]M. Nakayama, K. Miyazaki, T. Kawase, and D. Kim, Phys. Rev. B **83**, 075318 (2011).
[10]J. J. Hopfield and D. G. Thomas, Phys. Rev. **132**, 563 (1963).
[11]See http://www.mathworks.com/ for further information about the MATLAB programming environment.
[12]S. I. Pekar, Sov. Phys. Solid State **4**, 953 (1962).
[13]V. A. Kiselev, B. S. Razbirin, and I. N. Uraltsev, Phys. Status Solidi B **72**, 161 (1975).
[14]C. Schwab and A. Goltzene, Prog. Cryst. Growth Charact. Mater. **5**, 233 (1982).
[15]E. McGlynn, J. Fryar, M. O. Henry, J. P. Mosnier, J. G. Lunney, D. O'Mahony, and E. dePosada, Physica B **340**, 230 (2003).
[16]J. Fryar, E. McGlynn, M. O. Henry, and J. P. Mosnier, Nanotechnology **16**, 2625 (2005).
[17]J. Lagois, Phys. Rev. B **16**, 1699 (1977).
[18]O. Madelung, *Semiconductors: Data Handbook* (Springer, 2003), p. 911.
[19]E. Ostertag, Phys. Rev. Lett. **45**, 372 (1980).
[20]E. L. Ivhcenko, *Excitons*, edited by E. I. Rashba and M. D. Sturge (North-Holland, Amsterdam, 1982), p. 141.
[21]J. Munguía, J.-M. Bluet, H. Chouaib, G. Bremond, M. Mermoux, and C. Bru-Chevallier, J. Physics D: Appl. Phys. **43**, 255401 (2010).
[22]H. Akiyama, T. Kuga, M. Matsuoka, and M. Kuwata-Gonokami, Phys. Rev. B **42**, 5621 (1990).
[23]E. McGlynn, J. Fryar, G. Tobin, C. Roy, M. O. Henry, J. P. Mosnier, E. de Posada, and J. G. Lunney, Thin Solid Films **458**, 330 (2004).